ACS Photonics

Letter

pubs.acs.org/journal/apchd5

Direct Observation of Phase-Free Propagation in a Silicon Waveguide

Orad Reshef,[*,†,‡] Philip Camayd-Muñoz,[†] Daryl I. Vulis, Yang Li, Marko Lončar, and Eric Mazur

John A. Paulson School of Engineering and Applied Sciences, Harvard University, 9 Oxford Street, Cambridge, Massachusetts 02138, United States

Supporting Information

ABSTRACT: We demonstrate silicon waveguides that support phase-free propagation in the telecom regime. These waveguides have smaller footprints and exhibit improved energy transfer capabilities as compared to previous optical waveguides that support phase-advance-free modes. We measure the effective refractive index using on-chip interferometry and observe a zero-crossing around a wavelength of $\lambda = 1625$ nm. At this wavelength, we observe the coherent oscillations of waves that span the entire length of the waveguide. These waveguides are based on a 220-nm-thick silicon-on-insulator platform and, thus, are inherently compatible with established silicon photonic technologies.

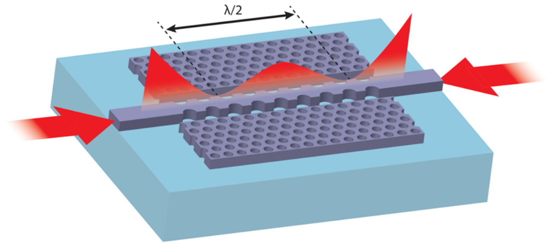

KEYWORDS: *silicon photonics, nanophotonics, metamaterials, zero refractive index, interferometry*

Optical waveguides provide a mechanism to tailor the characteristics of electromagnetic waves. Since the refractive index of propagating modes depends on the geometry of the waveguide, the design of nanostructured waveguides offers enormous flexibility for integrated optics. This ability to precisely define the refractive index and dispersion profile of an optical waveguide is critical to photonic applications, where dispersion engineering has been used to achieve slow light propagation[1−3] and plays a crucial role in determining phase-matching conditions for nonlinear optics.[4−9]

Nanostructuring can even push the index to extreme limits. Exotic physical phenomena emerge when the effective refractive index n_{eff} of a waveguide approaches zero. A material with a refractive index of zero exhibits an infinite wavelength and phase-free propagation.[10−12] These properties open up low-index media for applications in supercoupling,[12−14] in quantum optics,[15] and in beam-steering[16] and allow for dramatic nonlinear optical effects.[17−19] Phase-free propagation can be realized in photonic crystals[3,20] or plasmonic waveguides operating near the cutoff frequency.[21,22] However, such zero-index waves are accompanied by slow light effects associated with low power flow and poor coupling.[23] This connection is a consequence of the dispersion at cutoff, where the group velocity goes to zero, resulting in no energy transport.

Here, we present a zero-index platform in a corrugated silicon waveguide. These waveguides demonstrate phase-free propagation in the telecom regime ($\lambda = 1625$ nm) and exhibit excellent coupling to traditional dielectric waveguides (<0.15 dB/interface). To characterize the propagating modes, we perform on-chip interferometry and extract the effective index by directly imaging stationary waves using a standard free-space objective lens. Most strikingly, at the zero-index wavelength, we observe the coherent oscillations of waves that span the entire length of the waveguide. Measurements of transmission through these waveguides indicate efficient power transfer via the zero-index mode.

Our work is inspired by recent implementations of integrated Dirac-cone metamaterials.[24−30] Such metamaterials can be realized as two-dimensional slab structures monolithically structured from a standard silicon-on-insulator substrate and have been used to tune the effective refractive index down to arbitrarily small values, even crossing zero, while maintaining a finite group index.[28,29]

The waveguide consists of a single row of the zero-index metamaterial with a lattice constant of $a = 760$ nm and a cylindrical hole with a radius of $r = 212$ nm.[29] The unit cell from ref 29 is reconfigured to place the hole at its sides, resulting in a corrugated waveguide (Figure 1a). Eigenmode analysis of the waveguide (Figure 1b) yields a single propagating mode with an effective refractive index that transitions smoothly through zero with a finite group index due to the presence of both electric and magnetic dipole resonances[31] (see Supporting Information, waveguide design). This configuration couples efficiently to standard silicon ridge waveguides, allowing efficient power transfer into zero-index modes. Because the modes in this structure operate above the light line, they exhibit moderate radiative losses. However, we may reduce the propagation loss of these waveguides by cladding them with photonic band gap materials (PBG) consisting of a periodic array of holes in a silicon slab (see Supporting Information, addition of PBG cladding).

Received: July 13, 2017

DOI: 10.1021/acsphotonics.7b00760

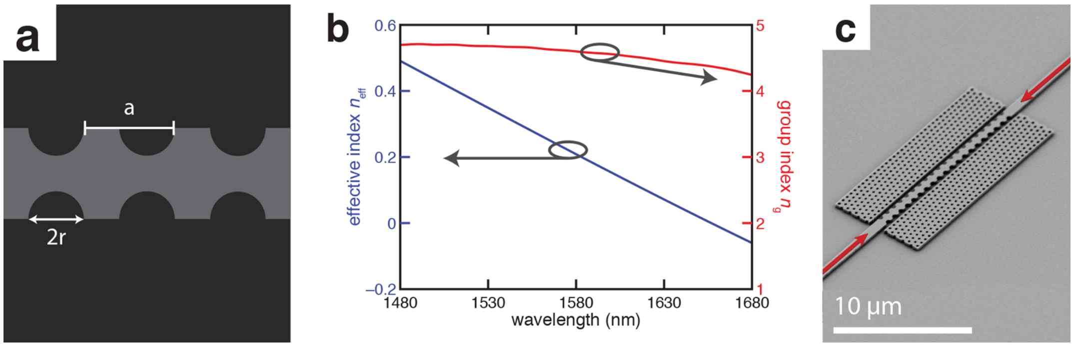

Figure 1. (a) Schematic of a silicon-based zero-index waveguide. (b) Simulated effective refractive index and group index for the zero-index waveguide. In contrast to other phase-free propagation structures, the group index remains finite throughout the wavelength operation range. (c) Scanning electron microscope image of a fabricated zero-index waveguide surrounded by a photonic band gap material.

The device is fabricated using standard planar fabrication methods for silicon photonic circuits (Figure 1c). We characterize the waveguide by measuring the propagation constant β of the guided mode, which can be expressed as a function of the effective refractive index $\beta = (2\pi n_{\mathrm{eff}}/\lambda)$. While there exist several methods to determine the index of bulk or planar metamaterials,[10,26,28,32] these approaches are not applicable to one-dimensional propagation. Characterization of such a structure typically relies on complex interferometric structures instead.[25,33,34] However, an elegant alternative is available when the index is sufficiently low ($|n|<1$): we may *directly* observe the effective wavelength by imaging a standing wave within the waveguide.[20,22]

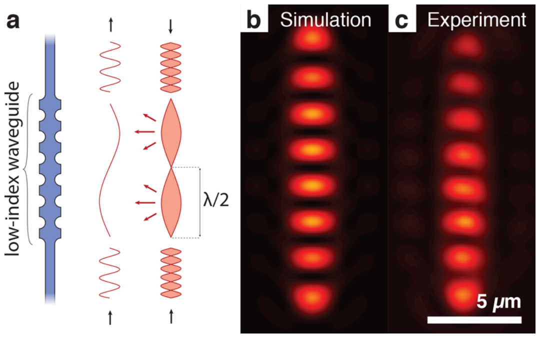

Figure 2. (a) A standing wave is formed when light enters coherently from both sides, which can be imaged directly in a low-index waveguide. The distance between the nodes in the standing wave is proportional to the effective wavelength. (b, c) Simulated and measured interference patterns obtained when illuminating a zero-index waveguide from both ends simultaneously with light at $\lambda = 1495$ nm.

We form a standing wave within the waveguide by exciting it on both ends simultaneously (Figure 2). The intensity formed by a pair of counter-propagating waves within a waveguide centered at $z = 0$ is found to be

$$I \propto \underbrace{\cos(2\beta z + \Delta\varphi)}_{\text{interference}} + \underbrace{\cosh(2\alpha z)}_{\text{background}} \qquad (1)$$

where z is the propagation distance, $\Delta\varphi$ is the relative phase between the two waves, and α is the propagation loss. The first term represents the interference of the waves, while the second term corresponds to the incoherent background intensity. The resulting standing wave features regularly spaced nodes separated by a distance corresponding to $\Delta z = (\lambda_0/2n_{\mathrm{eff}})$. Since n_{eff} is typically larger than 1, the distance between successive nodes or antinodes is usually a fraction of the free-space wavelength and, therefore, below the Abbe diffraction limit ($\approx \lambda/2$).[35] In a low-index material, however, the effective wavelength is larger than the free-space wavelength, expanding subwavelength features to macroscopic scales and producing optical frequency standing waves that are resolvable using a standard free-space objective lens.

By imaging a zero-index waveguide clad with PBG from above, we experimentally observe standing waves that closely resemble the predictions from 3D full-wave simulations (Figure 2b,c). Identical standing waves are also observed in zero-index waveguides without PBG. We extract an effective wavelength from this standing wave, and thus the magnitude of the effective index, by measuring the distance between consecutive nodes in these standing waves (see Supporting Information, image analysis).

We repeat this measurement for input wavelengths ranging from 1480 to 1680 nm to reconstruct the waveguide dispersion profile (Figure 3; for more, see Supporting Information, broadband interference spectrum). At short operating wavelengths, the standing waves have closely spaced nodes, corresponding to a short effective wavelength (i.e., high refractive index). As the wavelength increases, the node separation grows until a single antinode spans the entire waveguide around $\lambda = 1625$ nm. This trend is reversed for longer excitation wavelengths: the node separation decreases as wavelength increases. Since the standing wave evolves continuously as the wavelength is varied, we interpret these results as the dispersion of the effective index. Because this measurement is based on the effective wavelength, we are unable to distinguish between positive- and negative-index modes. However, we know from the simulation presented in Figure 1b that the waveguide mode has a positive refractive index for short wavelengths and negative index for long wavelengths. The dispersion profile extracted from the observed standing wave patterns agrees closely with the simulated index (Figure 4a). Both exhibit linear dispersion through zero index, crossing zero at approximately $\lambda = 1625$ nm. Thus, on-chip interferometry provides unambiguous confirmation of phase-free propagation.

Any direct observation of zero-index modes will be inherently limited by the extent of the guiding structure: when the effective wavelength becomes longer than twice the length of the waveguide, the standing wave patterns become indistinguishable from phase-free propagation. This size constraint is effectively a measurement floor, representing the

DOI: 10.1021/acsphotonics.7b00760
ACS Photonics XXXX, XXX, XXX−XXX

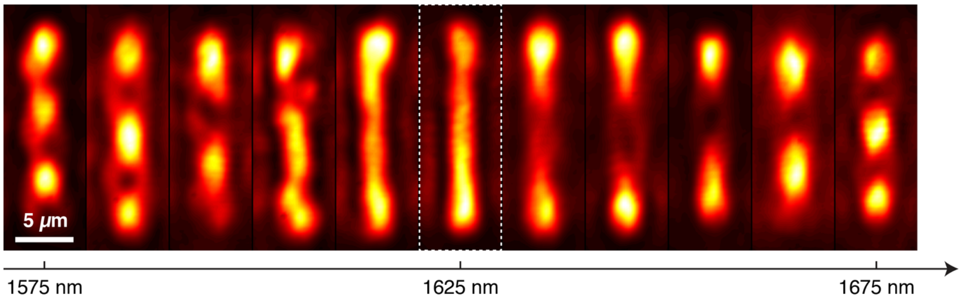

Figure 3. Distance between the nodes increases as the operating wavelength approaches the zero-index wavelength (λ = 1627 nm).

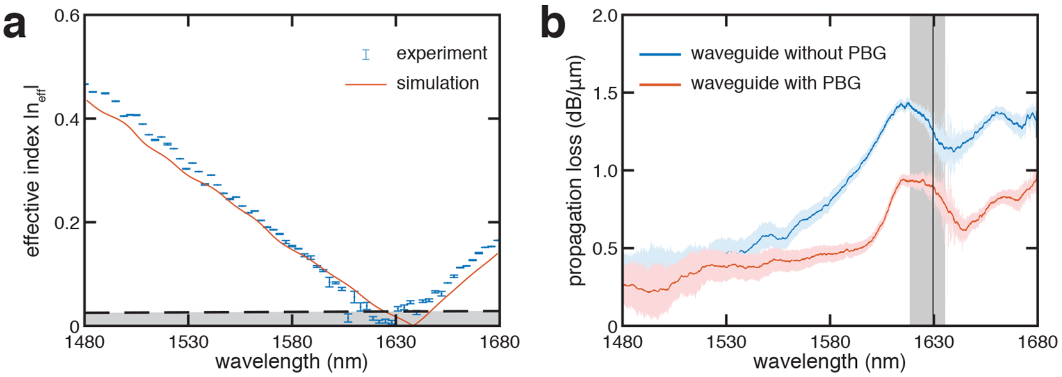

Figure 4. (a) The absolute value of the effective refractive index of a zero-index waveguide attains a value near zero at λ = 1627 nm, in good agreement with simulated extracted indices. The error bars correspond to 95% confidence intervals yielded by the fit. The black dashed line indicates the minimum effective index that can be measured using a 15-μm-long waveguide. (b) Propagation loss of zero-index waveguides. At the zero-index wavelength (indicated by the vertical black line), the addition of a PBG cladding reduces the propagation loss by 30%. The region shaded in gray corresponds to the wavelengths for which the index is measured to be below the limit indicated in (a).

minimum resolvable refractive index, which is indicated by the gray-shaded regions in Figure 4. The measured index is $|n_{eff}| \leq 0.03$ for 18 nm surrounding λ = 1627 nm. The absence of a band gap allows waves to propagate with finite group velocity and power flow even at the Γ-point.

We can quantify the power flowing in the zero-index mode by measuring the transmission through waveguides of various lengths. This allows us to estimate the propagation loss (Figure 4b) using a cutback analysis.[36] We perform the measurement for both clad and unclad waveguides and obtain propagation losses of 0.89 and 1.26 dB/μm, respectively, at the wavelength where n_{eff} = 0 (see Supporting Information, propagation losses). As there are no absorptive materials, the remaining propagation loss in clad waveguides corresponds to out-of-plane radiative coupling with continuum modes above the light line. Notably, the transmission is unchanged, and the propagation loss remains finite at the refractive index zero-crossing, providing further evidence for the lack of a band gap and corresponding slow light effects, respectively.

We have experimentally demonstrated waveguides that support phase-advance-free propagation modes based on the standard silicon-on-insulator platform. Through simultaneous electric and magnetic resonances, these modes maintain a finite group velocity even as the refractive index approaches zero, resulting in efficient power coupling to conventional dielectric waveguides. Although the current implementation is limited by propagation loss, the loss can be eliminated by creating a bound state in continuum,[37,38] which would facilitate applications in nonlinear optics. Due to its small footprint, this design is suitable for dense integration with silicon photonic circuits.

We determine the magnitude of the effective refractive index using an innovative on-chip interferometry method in which we directly image counter-propagating waves. This method is suitable for low-index devices of arbitrary shapes and can be implemented in situ without requiring additional interferometric circuitry. This experiment constitutes an additional independent proof that Dirac-cone metamaterials possess an effective refractive index of zero.

This one-dimensional implementation of zero-index metamaterials promises to expand the silicon photonics toolkit by extending the attainable values for the effective refractive index of a waveguide beyond what is conventionally permitted. Rather than a narrow range between the index of the core and the cladding, the refractive index of the waveguide can extend to values below the index of the cladding, including zero and even negative values. The design methodology outlined above can be used to extend these properties to any other desired material platform and to different operating wavelengths. Such metawaveguides provide unprecedented control over dispersion at the nanoscale.

■ ASSOCIATED CONTENT

Ⓢ Supporting Information

The Supporting Information is available free of charge on the ACS Publications website at DOI: 10.1021/acsphotonics.7b00760.

Additional text with extra information on the experimental methods, the device design methodology, integration with the PBG cladding, additional discussion on propagation losses, the image analysis method, additional measurements and a description of the appended visualizations (Figures S1–S6) (PDF)

Visualization 1: Real-time unprocessed video taken with an infrared camera of standing waves in a 15-μm-long zero-index waveguide at a wavelength of 1670 nm (AVI)

Visualization 2: Same device at an operating wavelength of 1650 nm (AVI)

Visualization 3: Same device at an operating wavelength of 1630 nm (AVI)

AUTHOR INFORMATION

Corresponding Author

*E-mail: orad@reshef.ca.

ORCID

Orad Reshef: 0000-0001-9818-8491

Philip Camayd-Muñoz: 0000-0002-1203-3083

Daryl I. Vulis: 0000-0002-9225-2621

Yang Li: 0000-0002-2146-6155

Eric Mazur: 0000-0003-3194-9836

Present Address

‡Department of Physics, University of Ottawa, 25 Templeton Street, Ottawa, Ontario K1N 6N5, Canada.

Author Contributions

O.R. and P.C.M. conceived the basic idea for this work. O.R., P.C.M., D.V., and Y.L. performed the simulations, O.R. performed the fabrication and carried out the experiments, and P.C.M. analyzed the results. E.M. and M.L. supervised the research and the development of the manuscript. O.R. and P.C.M. wrote the first draft of the manuscript; all authors subsequently took part in the revision process and approved the final copy of the manuscript.

Author Contributions

†O. Reshef and P. Camayd-Muñoz contributed equally to this work.

Notes

The authors declare no competing financial interest.

ACKNOWLEDGMENTS

The authors thank M. J. Burek for help with measurements. The research described in this article was supported by the National Science Foundation (NSF) under contract DMR-1360889. O.R. acknowledges the support of the Banting Postdoctoral Fellowship of the Natural Sciences and Engineering Research Council of Canada (NSERC). This work was performed in part at the Center for Nanoscale Systems (CNS), a member of the National Nanotechnology Coordinated Infrastructure Network (NNCI), which is supported by the National Science Foundation under NSF award no. 1541959. CNS is part of Harvard University.

REFERENCES

(1) Notomi, M.; Yamada, K.; Shinya, A.; Takahashi, J.; Takahashi, C.; Yokohama, I. Extremely large group velocity dispersion of line-defect waveguides in photonic crystal slabs. *Phys. Rev. Lett.* **2001**, *87*, 253902.

(2) Joannopoulos, J. D.; Johnson, S. G.; Winn, J. N.; Meade, R. D. *Photonic Crystals*, 2nd ed.; Princeton University Press: Princeton, NJ, 2008.

(3) Schulz, S. A.; O'Faolain, L.; Beggs, D. M.; White, T. P.; Melloni, A.; Krauss, T. F. Dispersion engineered slow light in photonic crystals: a comparison. *J. Opt.* **2010**, *12*, 104004.

(4) Agrawal, G. P. *Nonlinear Fiber Optics*, 4th ed.; Academic Press: Boston, MA, 2007.

(5) Leuthold, J.; Koos, C.; Freude, W. Nonlinear silicon photonics. *Nat. Photonics* **2010**, *4*, 535–544.

(6) Okawachi, Y.; Saha, K.; Levy, J. S.; Wen, Y. H.; Lipson, M.; Gaeta, A. L. Octave-spanning frequency comb generation in a silicon nitride chip. *Opt. Lett.* **2011**, *36*, 3398–3400.

(7) Lan, S.; Kang, L.; Schoen, D. T.; Rodrigues, S. P.; Cui, Y.; Brongersma, M. L.; Cai, W. Backward phase-matching for nonlinear optical generation in negative-index materials. *Nat. Mater.* **2015**, *14*, 807–811.

(8) Gattass, R. R.; Svacha, G. T.; Tong, L.; Mazur, E. Supercontinuum generation in submicrometer diameter silica fibers. *Opt. Express* **2006**, *14*, 9408–9414.

(9) Foster, M. A.; Moll, K. D.; Gaeta, A. L. Optimal waveguide dimensions for nonlinear interactions. *Opt. Express* **2004**, *12*, 2880–2887.

(10) Valentine, J.; Zhang, S.; Zentgraf, T.; Ulin-Avila, E.; Genov, D. A.; Bartal, G.; Zhang, X. Three-dimensional optical metamaterial with a negative refractive index. *Nature* **2008**, *455*, 376–379.

(11) Liberal, I.; Engheta, N. Near-zero refractive index photonics. *Nat. Photonics* **2017**, *11*, 149–158.

(12) Silveirinha, M.; Engheta, N. Tunneling of electromagnetic energy through subwavelength channels and bends using ϵ-near-zero materials. *Phys. Rev. Lett.* **2006**, *97*, 157403.

(13) Silveirinha, M. G.; Engheta, N. Theory of supercoupling, squeezing wave energy, and field confinement in narrow channels and tight bends using ϵ-near-zero metamaterials. *Phys. Rev. B: Condens. Matter Mater. Phys.* **2007**, *76*, 245109.

(14) Hajian, H.; Ozbay, E.; Caglayan, H. Enhanced transmission and beaming via a zero-index photonic crystal. *Appl. Phys. Lett.* **2016**, *109*, 031105.

(15) Fleury, R.; Alù, A. Enhanced superradiance in epsilon-near-zero plasmonic channels. *Phys. Rev. B: Condens. Matter Mater. Phys.* **2013**, *87*, 201101.

(16) Memarian, M.; Eleftheriades, G. V. Dirac leaky-wave antennas for continuous beam scanning from photonic crystals. *Nat. Commun.* **2015**, *6*, 5855.

(17) Suchowski, H.; O'Brien, K.; Wong, Z. J.; Salandrino, A.; Yin, X.; Zhang, X. Phase mismatch-free nonlinear propagation in optical zero-index materials. *Science* **2013**, *342*, 1223–1226.

(18) Alam, M. Z.; De Leon, I.; Boyd, R. W. Large optical nonlinearity of indium tin oxide in its epsilon-near-zero region. *Science* **2016**, *352*, 795–797.

(19) Reshef, O.; Giese, E.; Alam, M. Z.; De Leon, I.; Upham, J.; Boyd, R. W. Beyond the perturbative description of the nonlinear optical response of low-index materials. *Opt. Lett.* **2017**, *42*, 3225.

(20) Lončar, M.; Nedeljković, D.; Pearsall, T. P.; Vučković, J.; Scherer, A.; Kuchinsky, S.; Allan, D. C. Experimental and theoretical confirmation of Bloch-mode light propagation in planar photonic crystal waveguides. *Appl. Phys. Lett.* **2002**, *80*, 1689–1691.

(21) Edwards, B.; Alù, A.; Young, M. E.; Silveirinha, M.; Engheta, N. Experimental verification of epsilon-near-zero metamaterial coupling and energy squeezing using a microwave waveguide. *Phys. Rev. Lett.* **2008**, *100*, 033903.

(22) Vesseur, E. J. R.; Coenen, T.; Caglayan, H.; Engheta, N.; Polman, A. Experimental verification of $n = 0$ structures for visible light. *Phys. Rev. Lett.* **2013**, *110*, 013902.

(23) Javani, M. H.; Stockman, M. I. Real and Imaginary Properties of Epsilon-Near-Zero Materials. *Phys. Rev. Lett.* **2016**, *117*, 1–6.

(24) Huang, X.; Lai, Y.; Hang, Z. H.; Zheng, H.; Chan, C. T. Dirac cones induced by accidental degeneracy in photonic crystals and zero-refractive-index materials. *Nat. Mater.* **2011**, *10*, 582–586.

(25) Moitra, P.; Yang, Y.; Anderson, Z.; Kravchenko, I. I.; Briggs, D. P.; Valentine, J. Realization of an all-dielectric zero-index optical metamaterial. *Nat. Photonics* **2013**, *7*, 791–795.

(26) Li, Y.; Kita, S.; Muñoz, P.; Reshef, O.; Vulis, D. I.; Yin, M.; Lončar, M.; Mazur, E. On-chip zero-index metamaterials. *Nat. Photonics* **2015**, *9*, 738–742.

(27) Jahani, S.; Jacob, Z. All-dielectric metamaterials. *Nat. Nanotechnol.* **2016**, *11*, 23–36.

(28) Kita, S.; Li, Y.; Camayd-Muñoz, P.; Reshef, O.; Vulis, D. I.; Day, R. W.; Mazur, E.; Lončar, M. On-chip all-dielectric fabrication-tolerant zero-index metamaterials. *Opt. Express* **2017**, *25*, 8326−8334.

(29) Vulis, D. I.; Li, Y.; Reshef, O.; Camayd-Muñoz, P.; Yin, M.; Kita, S.; Lončar, M.; Mazur, E. Monolithic CMOS-compatible zero-index metamaterials. *Opt. Express* **2017**, *25*, 12381−12399.

(30) He, X.-T.; Huang, Z.-Z.; Chang, M.-L.; Xu, S.-Z.; Zhao, F.-L.; Deng, S.-Z.; She, J.-C.; Dong, J.-W. Realization of Zero-Refractive-Index Lens with Ultralow Spherical Aberration. *ACS Photonics* **2016**, *3*, 2262−2267.

(31) Sakoda, K. Universality of mode symmetries in creating photonic Dirac cones. *J. Opt. Soc. Am. B* **2012**, *29*, 2770−2778.

(32) Lezec, H. J.; Dionne, J. A.; Atwater, H. A. Negative refraction at visible frequencies. *Science* **2007**, *316*, 430−432.

(33) Kocaman, S.; Aras, M. S.; Hsieh, P.; McMillan, J. F.; Biris, C. G.; Panoiu, N. C.; Yu, M. B.; Kwong, D. L.; Stein, A.; Wong, C. W. Zero phase delay in negative-refractive-index photonic crystal superlattices. *Nat. Photonics* **2011**, *5*, 499−505.

(34) O'Brien, K.; Lanzillotti-Kimura, N. D.; Suchowski, H.; Kante, B.; Park, Y.; Yin, X.; Zhang, X. Reflective interferometry for optical metamaterial phase measurements. *Opt. Lett.* **2012**, *37*, 4089−4091.

(35) Abbe, E. Beiträge zur Theorie des Mikroskops und der mikroskopischen Wahrnehmung. *Archiv für mikroskopische Anatomie* **1873**, *9*, 413−418.

(36) O'Faolain, L.; Schulz, S. A.; Beggs, D. M.; White, T. P.; Spasenović, M.; Kuipers, L.; Morichetti, F.; Melloni, A.; Mazoyer, S.; Hugonin, J. P.; Lalanne, P.; Krauss, T. F. Loss engineered slow light waveguides. *Opt. Express* **2010**, *18*, 27627−27638.

(37) Hsu, C. W.; Zhen, B.; Lee, J.; Chua, S.-L.; Johnson, S. G.; Joannopoulos, J. D.; Soljačić, M. Observation of trapped light within the radiation continuum. *Nature* **2013**, *499*, 188−91.

(38) Muñoz, P.; Kita, S.; Mello, O.; Reshef, O.; Vulis, D. I.; Li, Y.; Lončar, M.; Mazur, E. *Lossless Integrated Dirac-Cone Metamaterials*; CLEO: Applications and Technology: San Jose, CA, 2016; p JW2A.24.

Supplemental Materials: Direct observation of phase-free propagation in a silicon waveguide

Orad Reshef,[*,†,‡,¶] Philip Camayd-Muñoz,[†,‡] Daryl I. Vulis,[†] Yang Li,[†] Marko Lončar,[†] and Eric Mazur[†]

†*John A. Paulson School of Engineering and Applied Sciences, Harvard University, 9 Oxford Street, Cambridge, Massachusetts 02138, USA*

‡*These authors contributed equally to this work.*

¶*Current address: Department of Physics, University of Ottawa, 25 Templeton Street, Ottawa, Ontario K1N 6N5, Canada*

E-mail: orad@reshef.ca

- 10 pages
- 6 figures

Abstract

This document provides supplementary information to "Direct observation of phase-free propagation in a silicon waveguide." First, in Section S1 we describe the experimental methods for our work in detail (Simulation, fabrication and measurement, respectively). Next, we outline the design methodology for the zero-index waveguide and demonstrate phase-free propagation in a device without a PBG cladding (Section S2). Next, we describe how to integrate the PBG cladding with the waveguide and its effects on the waveguide modes (Section S3), followed by a discussion on propagation losses (Section S4). In Section S5 we outline our image analysis method for extracting the effective refractive index from standing wave patterns. In Section S6, we provide additional measurements from the rest of our wavelength operation range, including background-subtracted interference patterns. Finally, in Section S7, we reproduce a descriptive caption for the attached visualizations.

S1 Experimental methods

Simulation

All simulations reported in this article were performed using three-dimensional models and dispersive materials. The zero-index waveguide and PBG are designed using a commercial finite-element eigensolver (*COMSOL Multiphysics*). For the waveguide, we simulate a single unit cell of the metamaterial by applying Bloch boundary conditions along one direction of the unit cell and perfectly matched layers on the remaining boundaries. The band structures are calculated assuming real frequencies and complex wavevectors.[1,2] For the PBG, we apply Bloch boundary conditions along both in-plane directions. The field profiles are calculated using a commercial finite-difference time-domain solver (*Lumerical FDTD Solutions*).

Fabrication

We spin a layer of negative-tone resist (XR-1541 6%, Dow Corning) on a 220-nm silicon-on-insulator wafer. The pattern is written using electron-beam lithography. The sample is developed in tetramethylammonium hydroxide (TMAH) and the pattern is subsequently transferred to the silicon substrate using inductively-coupled plasma reactive ion etching in a SF_6:C_4F_8 atmosphere at a ratio of 13:8. Polymer coupling pads with large cross-sectional areas are fabricated at the ends of the waveguides by spinning a negative tone resist (SU-8, MicroChem) onto the fabricated structures and using e-beam lithography. The sample is then cleaved at both ends of the chip to prepare input facets.

Measurement

We use a tunable coherent light source and a 50/50 directional coupler to create two input sources. Using two fiber polarization controllers, we ensure that we excite the device with TE-polarized light. Tapered lensed fibers are used to couple into the polymer coupling pads. The image is collected into an infrared camera above the device using an objective lens with a numerical aperture of 0.55. We repeat the measurements for all wavelengths between $\lambda = 1480$ and 1680 nm.

S2 Waveguide design

The waveguide is inspired by previously demonstrated monolithic all-dielectric zero-index metamaterials (Fig. S1a).[3] The corrugated waveguide structure has a lattice constant $a = 760$ nm and a hole radius of $r = 212$ nm, and a film thickness of 220 nm. In the configuration of a two-dimensional square array photonic crystal slab, these dimensions produce a band structure that exhibits a photonic Dirac cone at the Γ-point for an operating wavelength of $\lambda = 1625$ nm. For the one-dimensional analog of this structure, such as the waveguide presented in this case, a Dirac cone at the Γ-point becomes a pair of bands with linear dispersion, intersecting at a propagation constant β of 0 (Fig. S1b). The high-frequency band propagates with a positive effective index, while the low-frequency band has a negative effective index (indicated by anti-parallel wavevector and Poynting vector in simulations). The hybrid mode at the intersection contains both an electric dipole as well as a magnetic dipole resonance in quadrature (Fig. S1c). By analogy to the 2-D metamaterial in Ref. 3, these mode symmetries provide the electric and magnetic responses that are necessary to obtain a finite impedance. Without this impedance, we would not be able to couple efficiently to silicon photonic waveguides, in contrast to other epsilon-near-zero (ENZ) materials.

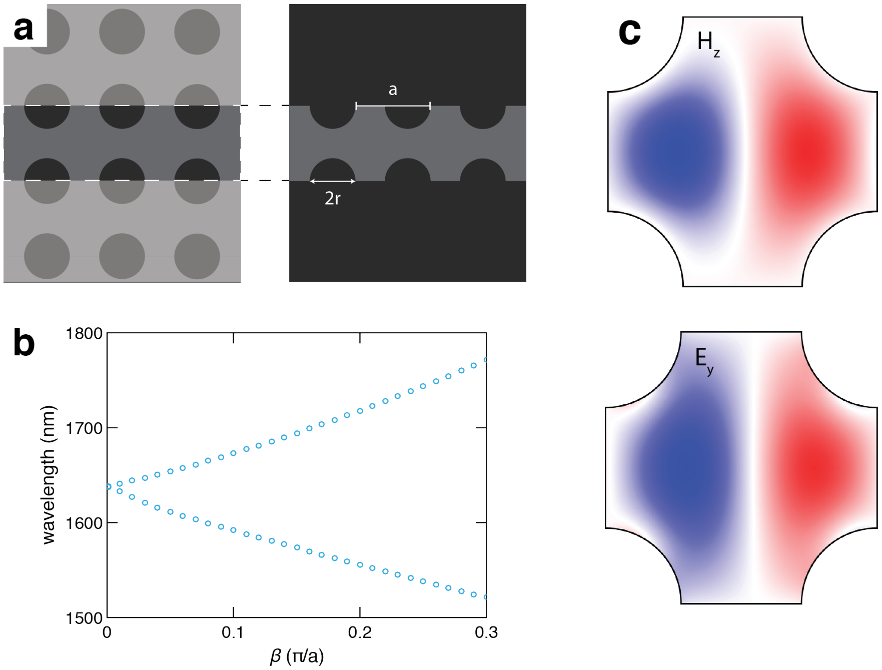

Figure S1: **a)** Schematic of zero-index waveguide consisting of a single-channel zero-index metamaterial. **b)** The band structure for this waveguide possesses a pair of modes that linearly intersect at the Γ-point ($\beta = 0$). For clarity, modes with a quality factor below 20 have been filtered out. **c)** The magnetic H-field perpendicular to the plane of the device (H_z) and the out-of-phase in-plane E-field (E_y) for the mode at the Γ-point.

We fabricate this device using the procedure described in the methods section (Fig. S2a). By performing the measurement and extraction procedure on these waveguides, we determine the absolute value of the effective refractive index for these devices using the method described in Section S5. We see an effective index zero-crossing near the design wavelength, at 1625 nm (Fig. S2b).

We conclude this section by noting that the measured and simulated dispersion curves shown here are identical to the waveguides that are clad with PBG as shown in Fig. 4a of the main text. Thus, the addition of PBG is not necessary to achieve linear dispersion.

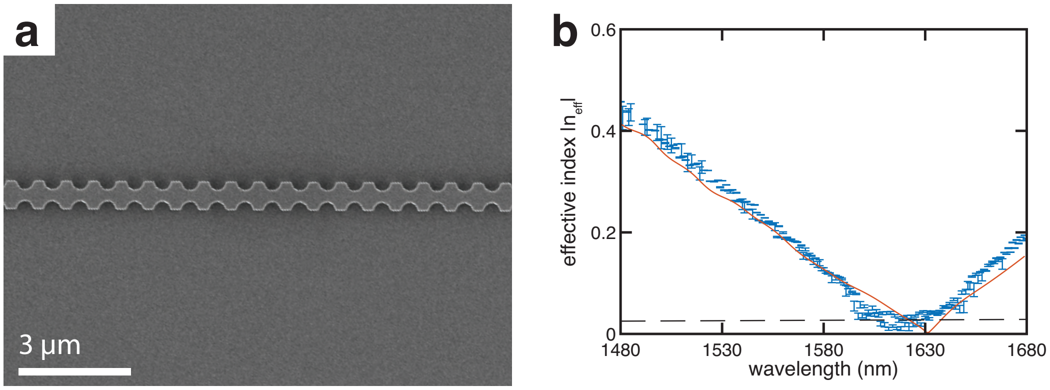

Figure S2: **a)** Fabricated zero-index waveguide. **b)** The effective refractive index approaches zero near $\lambda = 1626$ nm, in agreement with 3D simulations.

S3 Addition of photonic band gap cladding

Modes that operate above the light line, including zero-index modes, are susceptible to radiative coupling with continuum waves. Thus, a zero-index waveguide experiences significant propagation losses. Fortunately, such radiative losses (as opposed to roughness-induced scattering losses or absorption losses) can be mitigated if the emitted light is reflected and returned to the waveguide in-phase with the propagating mode.

We use a slab of photonic band gap (PBG) materials to serve as an on-chip reflector (Fig. S3). The PBG consists of a triangular lattice of holes with a lattice constant of $a_{\mathrm{PBG}} = 450$ nm, a hole radius of $r_{\mathrm{PBG}} = 124$ nm. This geometry integrates seamlessly with the waveguide, providing a PBG for all TE-polarized light for wavelengths ranging from $\lambda = 1410 - 1710$ nm.

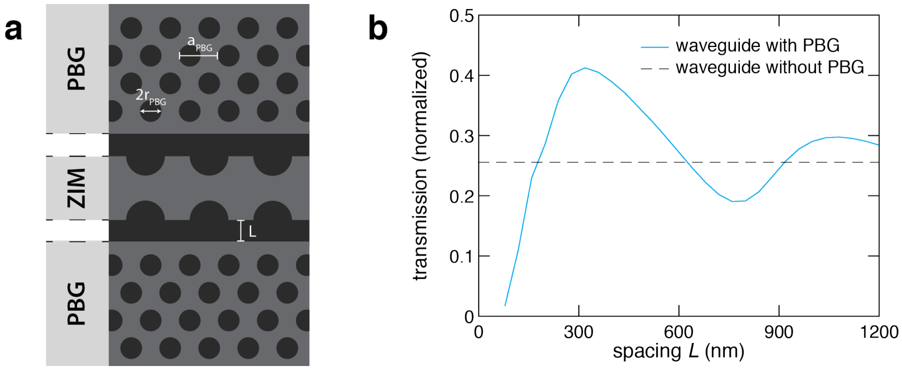

Figure S3: **a)** Schematic of a zero-index waveguide clad by photonic band gap materials. **b)** Normalized transmission through 6 unit cells of zero-index waveguide as a function of the spacing L between the PBG lattice and the zero-index waveguide. The PBG provides the strongest destructive interference at $L = 320$ nm, corresponding to the lowest propagation loss in the structure.

With the addition of PBG reflectors, the radiated waves become coupled with the zero-index mode. In order to preserve Dirac-like dispersion, the reflected light should be in-phase with the propagating mode. We control the phase of the reflected light by adjusting the spacing L between the PBG and the zero-index waveguide. An ideal reflector imparts a π phase shift upon reflection, so we expect the optimal spacing L for efficient power coupling to be approximately a quarter of the wavelength of light propagating in free space ($\lambda/4 \approx 400$ nm). To determine the optimal spacing for this configuration, we simulate the transmittance of the PBG-clad waveguide for different spacings L (Fig. S3b). Here, we see that the ideal length is $L = 320$ nm, and the propagation loss is reduced to 0.82 dB/µm, relative to the unclad case 1.22 dB/µm. Conversely, the transmission is reduced when the reflected light is out of phase with the propagating mode. The effect of the PBG diminishes as L is increased further since the PBG reflects a smaller portion of the radiative loss. Therefore, we select a spacing $L = 320$ nm to maximize power transmission.

S4 Propagation losses

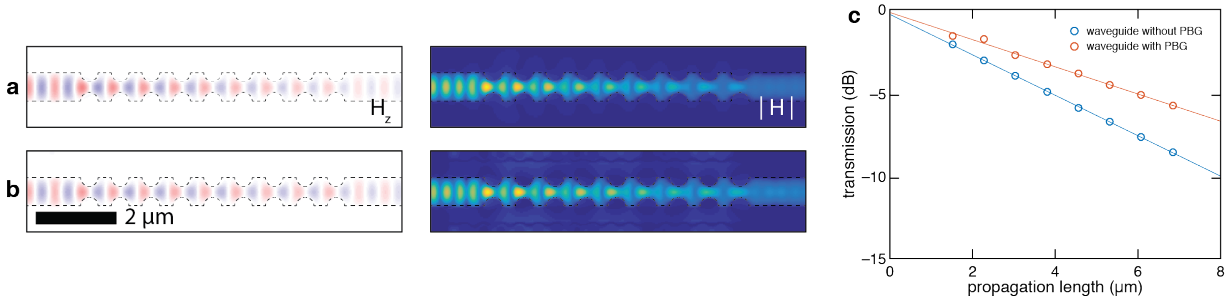

Figure S4: **a-b)** Simulation of the out-of-plane $\vec{H}$-field component and the magnitude of the field $|\vec{H}|$ for a zero-index waveguide without (a) and with (b) a PBG cladding when excited by a TE-polarized silicon waveguide. The outline of the waveguide is indicated by a dashed black line. **c)** Simulated propagation losses as determined by a virtual cutback method.

We use 3D full-wave simulations (FDTD) to characterize the performance of the PBG-clad waveguides. We start by exciting a zero-index waveguide with and without a PBG (Fig. S4a-b). The structure of the modes excited within the device is observed to be unchanged in the presence of PBGs. In both structures, the amplitude of the fields decreases due to propagation loss; however, light excited in the waveguide clad by PBGs decays more slowly.

To estimate the change in propagation loss quantitatively, we perform a virtual cutback measurement by simulating waveguides with $2-9$ pitches of zero-index waveguides with and without the PBG cladding (Fig. S4c). We fit to the transmitted output and extract a propagation loss of 1.22 dB/µm for the unclad waveguides, and a propagation loss of 0.82 dB/µm for the PBG-clad zero-index waveguides, corresponding to an improvement of over 30%. These values are in excellent agreement with the measured values, where the propagation losses were found to be 1.26 and 0.89 dB/µm for the unclad and clad waveguides, respectively. The coupling loss of 0.15 dB/interface is nearly identical for both devices, further confirming that the modes are not perturbed by the presence of the PBG.

To determine the propagation losses, we fabricate sets of zero-index waveguides with and without a PBG cladding. These devices contain zero-index regions of 5, 10, 15 and 20 unit cells, corresponding to waveguides with lengths of approximately 3.75, 7.5, 11.25 and 15 µm, respectively. We measure transmission through these devices from $\lambda = 1480$ to 1680 nm. Assuming that the coupling efficiencies are the same for all of the devices, this emulates a cutback measurement. We fit the transmission as a function of device length and extract a propagation loss, as shown in the main text in Fig. 4c. The PBG-clad waveguides outperform the unclad zero-index waveguides for nearly the entire operation range. At the zero-index wavelength, $\lambda = 1627$ nm, the unclad waveguide has a propagation loss of 1.26 dB/µm, whereas the clad waveguide has a propagation loss of 0.89 dB/µm, a 30% improvement. These values are in good agreement with the simulated ones.

S5 Image analysis

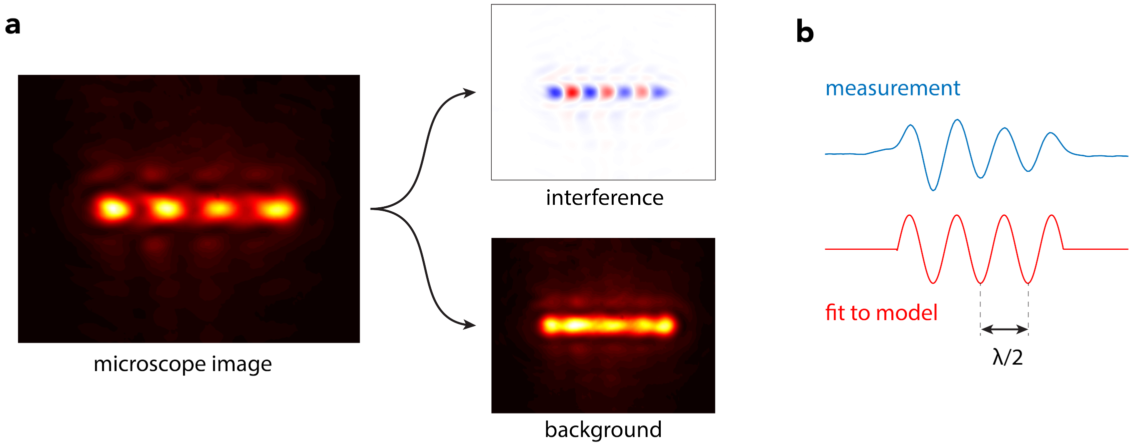

Figure S5: **Extracting effective index from microscope images.** a) Each frame is separated into background and interference components. b) The interference signal is fit to a truncated sinusoidal model to extract the effective wavelength λ of the propagating mode.

To experimentally measure the refractive index, we illuminate the zero-index waveguide from both ends using via a tapered fiber at each facet. This forms a standing wave within the waveguide, whose periodicity is equal to half of the effective wavelength. By imaging the waveguide from above, we are able to estimate the effective index of the propagating mode.

The standing wave is sensitive to vibrations that introduce random phase differences between the two input beams. While this does not change the period of the standing wave, it causes the pattern to shift laterally, as predicted by Eq. 1 (Visualizations 1-3). In order to improve the fidelity of the measurement we collect multiple images of the waveguide, each of which has a random relative phase due to vibrations of the input fibers. By comparing the ensemble of frames, we can control for these phase variations and estimate their common effective index.

The fitting procedure begins by isolating the interference signal from each frame: we average 50 individual frames to extract a background signal (Eq. 1) that represents the non-interference component of the standing wave, corresponding to the exponential decay of the input waves. Subtracting this background from each individual frame results in an interference pattern that depends only on the effective index and the relative phase of the input beams (Figure S5a). We fit interference signal to a windowed sinusoidal wave, with free parameters for the phase and effective index (Figure S5b). This process allows us to estimate the effective index with high precision. In addition, the analysis reveals that the relative phase is randomly distributed across all frames, validating the original hypothesis. Using this method, we estimate the effective index at different input wavelengths ranging from 1480 nm – 1680 nm, with a wavelength resolution of 1 nm.

S6 Broadband interference spectrum

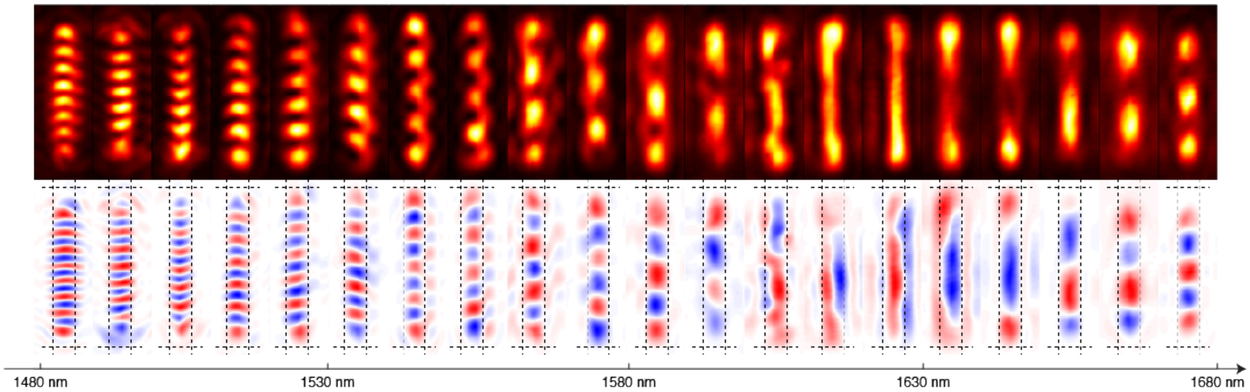

Figure S6: Interference pattern obtained from the device in Fig. S1 when illuminated at both ends simultaneously. The waveguide is outlined by a dashed black line. The distance between the nodes increases as the operating wavelength approaches the zero-index wavelength ($\lambda = 1627$ nm).

In order to completely describe the behavior of our zero-index device, here we reproduce the interference patterns in a zero-index waveguide for the entire wavelength operation range ($\lambda = 1480$ nm – 1680 nm). We also display the corresponding isolated interference signals described in Section S5. It is clear that the magnitude of the effective wavelength is small at frequencies far from the zero-index wavelength, and increases as we approach the device's zero-index wavelength from either side.

S7 Caption for visualizations

Real-time unprocessed video taken with an infrared camera of standing waves in a 15-μm-long zero-index waveguide at wavelengths of 1670 nm (Visualization 1), 1650 nm (Visualization 2), and 1630 nm (Visualization 3), corresponding to effective indices of -0.01, -0.06, and 0.14, respectively. The perceived motion is caused by atmospheric disturbances to the free-standing fibers that couple light onto the chip, changing the relative phase between the two incoming beams.

References

(1) Davanco, M.; Urzhumov, Y.; Shvets, G. *Opt. Express* **2007**, *15*, 9681–9691.

(2) Fietz, C.; Urzhumov, Y.; Shvets, G. *Opt. Express* **2011**, *19*, 19027–19041.

(3) Vulis, D. I.; Li, Y.; Reshef, O.; Camayd-Muñoz, P.; Yin, M.; Kita, S.; Lončar, M.; Mazur, E. *Opt. Express* **2017**, *25*, 12381–12399.